AD-A174 321 THE VARIATION OF SUBGRAIN MISORIENTATION IN ALUMINUM 1/1
WITH LARGE STEADY-STATE CREEP STRAIN(U) NAVAL
POSTGRADUATE SCHOOL MONTEREY CA M E MCMAHON JUN 86
UNCLASSIFIED F/G 11/6 NL

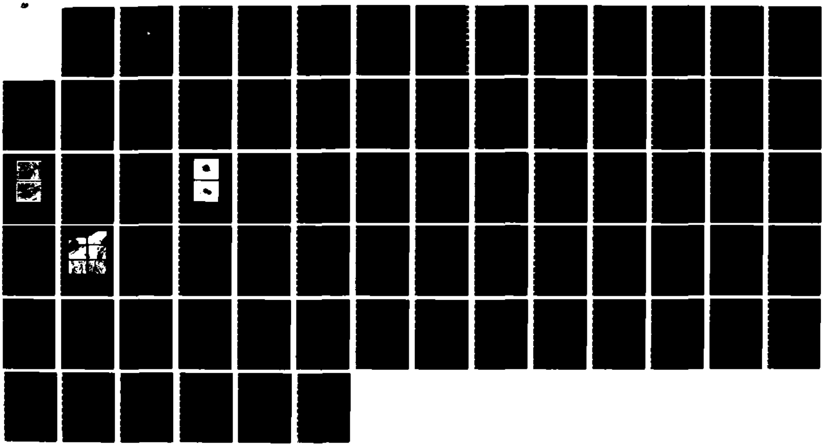

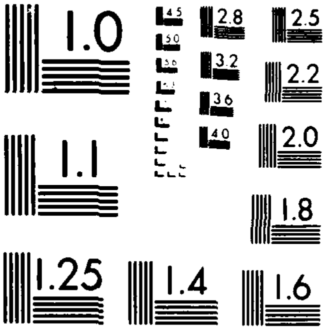

MICROCOPY RESOLUTION TEST CHART
NATIONAL BUREAU OF STANDARDS-1963-A

2

NAVAL POSTGRADUATE SCHOOL

Monterey, California

THESIS

THE VARIATION OF SUBGRAIN MISORIENTATION IN ALUMINUM WITH LARGE STEADY-STATE CREEP STRAIN

by

Michael E. McMahon

June 1986

Thesis Advisor: M. E. Kassner

Approved for public release; distribution is unlimited.

AD-A174321

SECURITY CLASSIFICATION OF THIS PAGE

REPORT DOCUMENTATION PAGE

1a. REPORT SECURITY CLASSIFICATION
UNCLASSIFIED

1b. RESTRICTIVE MARKINGS

2a. SECURITY CLASSIFICATION AUTHORITY

2b. DECLASSIFICATION / DOWNGRADING SCHEDULE

3. DISTRIBUTION / AVAILABILITY OF REPORT
Approved for public release; distribution is unlimited

4. PERFORMING ORGANIZATION REPORT NUMBER(S)

5. MONITORING ORGANIZATION REPORT NUMBER(S)

6a. NAME OF PERFORMING ORGANIZATION
Naval Postgraduate School

6b. OFFICE SYMBOL (If applicable)
Code 69

7a. NAME OF MONITORING ORGANIZATION
Naval Postgraduate School

6c. ADDRESS (City, State, and ZIP Code)
Monterey, California 93943-5000

7b. ADDRESS (City, State, and ZIP Code)
Monterey, California 93943-5000

8a. NAME OF FUNDING / SPONSORING ORGANIZATION

8b. OFFICE SYMBOL (If applicable)

9. PROCUREMENT INSTRUMENT IDENTIFICATION NUMBER

8c. ADDRESS (City, State, and ZIP Code)

10. SOURCE OF FUNDING NUMBERS

PROGRAM ELEMENT NO.	PROJECT NO.	TASK NO.	WORK UNIT ACCESSION NO.

11. TITLE (Include Security Classification)
THE VARIATION OF SUBGRAIN MISORIENTATION IN ALUMINUM WITH LARGE STEADY-STATE CREEP STRAIN

12. PERSONAL AUTHOR(S)
McMahon, Michael E.

13a. TYPE OF REPORT
Master's Thesis

13b. TIME COVERED
FROM ________ TO ________

14. DATE OF REPORT (Year, Month, Day)
1986 June

15. PAGE COUNT
73

16. SUPPLEMENTARY NOTATION

17. COSATI CODES

FIELD	GROUP	SUB-GROUP

18. SUBJECT TERMS (Continue on reverse if necessary and identify by block number)
Subgrain, Dislocation, Misorientation, Network, Creep, Steady-State, Geometric-Dynamic-Recrystallization

19. ABSTRACT (Continue on reverse if necessary and identify by block number)

High purity aluminum was torsionally deformed to various strains up to 16.33 at a temperature of 644 K in this study. The variation in the dislocation substructure was determined with increasing strain. Recent work revealed that both the subgrain size and density of dislocations not associated with subgrain boundaries remained constant over the range of steady-state strains examined. However, transmission electron microscopy in this work revealed that subgrain boundaries undergo two types of basic changes during steady-state creep. At the onset of steady-state behavior ($\varepsilon = 0.20$) all subgrain boundaries had small misorientations, typically, 0.6°. The misorientation across boundaries formed as a result of dislocation accumulation continued to increase well past steady-state up to a strain of about 1.2, where a maximum average value of 1.2° was observed. This suggests that (continued)

20. DISTRIBUTION / AVAILABILITY OF ABSTRACT
☒ UNCLASSIFIED/UNLIMITED ☐ SAME AS RPT. ☐ DTIC USERS

21. ABSTRACT SECURITY CLASSIFICATION
UNCLASSIFIED

22a. NAME OF RESPONSIBLE INDIVIDUAL
Michael E. Kassner

22b. TELEPHONE (Include Area Code)
408-646-3036

22c. OFFICE SYMBOL
69KM

DD FORM 1473, 84 MAR

83 APR edition may be used until exhausted.
All other editions are obsolete.

SECURITY CLASSIFICATION OF THIS PAGE

19. (Continued)

the dislocation spacing in subgrain boundaries is not principally responsible for the creep resistance during five power-law creep. At strains greater than about four, nearly a third of the subgrain boundaries were determined to be high angle boundaries (HAB). Polarized light microscopy revealed that the large fraction of HAB's observed was a result of a geometric dynamic recrystallization consistent with that discussed by McQueen and coworkers. The boundaries formed from dislocation reaction rarely develop misorientations greater than 3°. The increased presence of the high angle boundaries during steady-state where a constant subgrain size and constant forest dislocation density structure are observed also suggests that the misorientation of subgrains is not an important microstructural feature.

The Variation of Subgrain Misorientation in Aluminum with Large Steady-State Creep Strain

by

Michael E. McMahon
Lieutenant, United States Navy
B.S., University of Colorado, 1979

Submitted in partial fulfillment of the
requirements for the degree of

MASTER OF SCIENCE IN MECHANICAL ENGINEERING

from the

NAVAL POSTGRADUATE SCHOOL
June 1986

Author: ______________________________
Michael E. McMahon

Approved by: ______________________________
M. E. Kassner, Thesis Advisor

PJ Marto
____
Paul J. Marto, Chairman
Department of Mechanical Engineering

JN Dyer
____
John N. Dyer, Dean of Science and Engineering

ABSTRACT

High purity aluminum was torsionally deformed to various strains up to 16.33 at a temperature of 644 K in this study. The variation in the dislocation substructure was determined with increasing strain. Recent work revealed that both the subgrain size and density of dislocations not associated with subgrain boundaries remained constant over the range of steady-state strains examined. However, transmission electron microscopy in this work revealed that subgrain boundaries undergo two types of basic changes during steady-state creep. At the onset of steady-state behavior ($\epsilon = 0.20$) all subgrain boundaries had small misorientations, typically, 0.6°. The misorientation across boundaries formed as a result of dislocation accumulation continued to increase well past steady-state up to a strain of about 1.2, where a maximum average value of 1.2° was observed. This suggests that the dislocation spacing in subgrain boundaries is not principally responsible for the creep resistance during five power-law creep. At strains greater than about four, nearly a third of the subgrain boundaries were determined to be high angle boundaries (HAB). Polarized light microscopy revealed that the large fraction of HAB's observed was a result of a geometric dynamic recrystallization consistent with that discussed by McQueen and coworkers. The boundaries formed from dislocation reaction rarely develop misorientations

greater than 3°. The increased presence of the high angle boundaries during steady-state where a constant subgrain size and constant forest dislocation density structure are observed also suggests that the misorientation of subgrains is not an important microstructural feature.

TABLE OF CONTENTS

LIST OF FIGURES

ACKNOWLEDGEMENT

I would like to express thanks to my thesis advisor, Professor M. E. Kassner, for his professional guidance and support during the course of this research. Appreciation is also expressed to Dr. Prabir Deb for his technical assistance and to Mr. C. J. Echer of Lawrence Berkeley Laboratory for contributing his knowledge and skill of transmission electron microscopy.

I. INTRODUCTION

This work was the last part of a larger study conducted to determine the rate-controlling mechanism of high temperature creep in 99.999% pure aluminum. The research was initiated by the absence of a comprehensive high temperature creep study that evaluated the dislocation microstructure over a very wide range of steady-state strain. Insight into the rate controlling process of creep is gained by observing the variation in the subgrain size, λ, the density of dislocations not associated with subgrain boundaries, ρ, and the spacing of dislocations that compose the subgrain boundaries, d (related to the misorientation across the boundaries, θ) with steady-state strain. In this part of the study, the role of subgrain boundaries during high temperature creep was determined by measurement of the variation in the dislocation spacing in the sub-boundary and subgrain misorientation with steady-state strain using transmission electron microscopy. Research that identifies the strengthening mechanism of metals during high temperature creep will contribute to the development of constitutive equations to predict material properties during long-term high temperature service applications.

II. BACKGROUND

A. THEORETICAL

Creep of metals and alloys is a thermally activated process that occurs at temperatures greater than about half of the absolute melting temperature (0.5 T_m). Here, the activation energy for creep, Q_c, is approximately equal to the activation energy for self diffusion [Ref. 1]. When metals are deformed at these temperatures, random (forest) dislocations are produced. Due to the increased atomic mobility at elevated temperatures, some of the forest dislocations form dislocation tangles that eventually form characteristic three-dimensional low-energy configurations which are subgrain boundaries. In face centered cubic (FCC) metals, the dislocation network is thought [Refs. 2, 3] to consist of several (2-5) distinct sets of dislocations in a nodal array.

Figure 2.1 [Refs. 4, 5] illustrates the stress versus strain behavior of a typical subgrain forming metal or alloy during constant strain-rate deformation at an elevated temperature. Three distinct regions of creep behavior are evident. During primary creep, hardening is associated with an increase in forest dislocation density and the eventual formation of subgrains. Secondary creep or steady-state

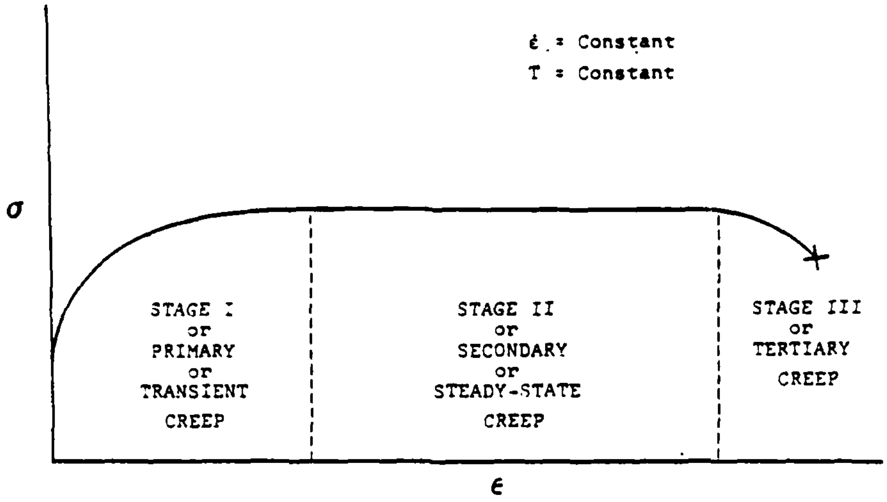

Figure 2.1: Typical elevated temperature stress-strain behavior of a subgrain forming metal during constant strain rate deformation.

creep is characterized by approximately constant flow stress for a constant strain-rate test. Hardening effects are balanced by recovery processes during steady-state. In the past, it was generally believed that the microstructure of the metal does not change during steady-state. In this range, the creep rate has been shown [Ref. 1] to obey the "power-law" relation:

$$\dot{\varepsilon}_{ss} = A\ D\ \gamma^{3.5}\ (\sigma/E)^{n} \qquad (2\text{-}1)$$

or equivalently:

$$\sigma = E \left[\frac{\dot{\varepsilon}_{ss}}{A\ D\ \gamma^{3.5}} \right]^{1/n} \qquad (2\text{-}2)$$

where γ is the stacking fault energy, E is the modulus of elasticity, $\dot{\epsilon}_{ss}$ is the steady-state creep rate, D is the coefficient of self diffusion, σ is the flow stress, A is the constant, and N approximately equal to 5 for pure metals. In tertiary creep, the relation:

$$\dot{\epsilon} = K e^{B\sigma} \tag{2-3}$$

is thought [Ref. 1] to describe the creep rate up to rupture, where K and B are constants. Inspection of Eq. (2.1) reveals that several parameters [Ref. 1] affect the steady-state behavior of subgrain forming metals and alloys at elevated temperatures. Decreasing the diffusion coefficient, for example, corresponds to inhibiting atomic mobility and the creep rate will be reduced, effectively strengthening the metal. Stacking fault energy determines the distance that partial or extended dislocations must contract for dislocation climb or cross-slip to occur. Lower stacking fault energy would inhibit these recovery processes and increase creep resistance. The dislocation substructure also affects the elevated temperature strength of a metal. The substructure consists of the subgrain size, λ, the density of dislocations not associated with subgrain boundaries or forest dislocations, ρ, and the spacing of dislocations that compose the subgrain boundaries, d, which is related to the misorientation angle across subgrain boundaries. The subgrains may strengthen in a manner analogous to grain size strengthening described by the Hall-Petch relation and forest dislocations by obstacle strengthening by a Taylor type relation.

Subgrain boundary dislocations have been proposed [Ref. 3] to affect creep resistance in one of the following ways:

(1) The dislocation separation distance determines the effectiveness of subgrain boundaries as obstacles to gliding dislocations.

(2) The distance between dislocations in the sub-boundary determines the distance that dislocations must climb to annihilate and allow subsequent dislocation glide.

(3) The distance between dislocations influences the stress required to emit dislocations from the subgrain boundary.

(4) The distance between dislocations influences the effective stress near the subgrain boundaries.

Subgrain boundaries exist as dislocation tilt, screw, or mixed boundaries with typical misorientations of 0.5° - 3.0°. For a pure tilt or pure twist boundary, the relation:

$$\theta = b / d \tag{2-4}$$

[Ref. 3] applies where b is the Burgers vector (b = .286 nm for aluminum), d is the dislocation separation in the subgrain boundary and θ is the subgrain boundary misorientation in radians.

The flow stress is independent of strain during secondary stage creep for a constant strain-rate test. It is expected, then, that the microstructural feature associated with the creep process would remain constant throughout the secondary creep range since any significant strengthening feature is expected to be reflected by changes in the flow stress. Therefore, one way to determine the microstructural feature associated with the rate controlling process of creep is to examine the variation of the three microstructural features with steady-state strain. The features that change can be eliminated. Unfortunately, reasonable steady-state strains cannot be achieved by conventional tension tests because of failure. The range of testing strain can be dramatically extended by utilizing torsion tests. However, large steady-state deformation may have some complications.

It has been found in a few investigations [Ref. 6] that relatively large strain deformation, as can result from torsion tests, is associated with an increased number of high angle boundaries. The evolution of these boundaries has been debated. It has been proposed [Refs. 7-9] that subgrain boundaries, formed as a result of accumulation of dislocations created during creep, are responsible for a continous recrystallization within the metal. Formation of new grains in this manner is thought to occur, in one theory, as a result of subgrain coalesence. In this theory, dislocations are thought to migrate from disappearing, low misorientation, subgrain boundaries to nearby high angle boundaries, which act as dislocation sinks. As a result, subgrains rotate and the misorientation across the remaining boundaries increases. Another possibility is that the existing boundaries continually absorb dislocations and the misorientation gradually increases to eventually form high angle boundaries.

Other recent theories [Ref. 6] have described the formation of high angle boundaries during large plastic deformation as geometric dynamic recrystallization. Here, high angle grain boundaries are serrated as a result of the formation of low angle subgrain boundaries. As the specimen is torsionally deformed, the boundaries spiral about the torsion axis until the axial width of the original grains is reduced to the order of the size of the subgrains formed early in the deformation process. The effect of these high angle boundaries in high temperature creep is not known.

B. PREVIOUS RESEARCH

Research to determine the microstructural feature associated with the rate controlling mechanism of creep has utilized [Ref. 2] x-ray topography, transmission and scanning electron microscopy, etch-pitting techniques, and optical microscopy, in conjunction with a variety of mechanical tests. The results are inconclusive. The present approach is to observe the variation of λ, ρ, and particularly d (θ) as a function of steady-state strain. Some other investigations have done this but with conflicting results.

Research by Orlova, Tobolova, and Cadek [Ref. 10] on high temperature creep in high purity aluminum suggested that the dislocation substructure reached steady-state very soon after loading ($\epsilon = 0.20$). Excell and Warrington [Ref. 11] used x-ray topography to measure subgrain size and subboundary misorientation during high temperature creep testing of 99.999% pure aluminum and found that misorientation increased to a strain of 0.05, but attained an approximately constant value at the onset of steady-state. It was concluded that the subgrain boundaries may harden the metal by acting as an obstacle to gliding dislocations or by becoming bowed, reducing the overall effective stress in the metal due to a back stress. These investigators concluded that a constant subgrain size during steady-state is the result of a balance between subgrain boundary formation and subgrain boundary migration and annihilation. Several other investigations [Refs. 12-14] also conclude that λ, ρ, and d (and θ) are fixed during steady-state.

Work by Suh, Cohen, and Weertman [Ref. 15], however, on single crystals of tin creep tested at .84 T_m concluded that subgrain boundary misorientation increased continuously throughout steady-state, suggesting that the details of the subgrain boundary where not important in strengthening. The misorientation appeared to linearly increase with strain, suggesting that high angle boundaries may eventually form.

Elevated temperature creep research conducted by Morris and Martin [Ref. 16] on aluminum-11 wt.% zinc also found that d decreased, linearly, during steady-state. They suggested, however, that the effective stress at sub-boundaries was inversely related to the mesh size and that the stress necessary to eject dislocations from the boundary is also inversely proportional to the spacing. They suggest that steady-state is maintained despite a decrease in the spacing of dislocations, then, by a compensation of these two effects.

Petry and Pschenitzka [Ref. 17] reported creep tests results for aluminum-11 wt.% zinc at a constant stress of 15.4 MPa and a temperature of 523 K. The subgrain size was found to decrease up to the onset of steady-state ($\epsilon = 0.20$) and remain constant thereafter. Spacing of dislocations in subgrain boundaries, however, was found to decrease well into the steady-state region although a limiting or "saturation" value was achieved during steady-state.

One limitation to many of the studies, however, is the absence of the significant plastic strain required to fully evaluate behavior throughout steady-state since torsion tests were not utilized. A recent comprehensive study of type 304 stainless steel by Kassner and Elmer [Ref. 3] examined the variation of these three substructural features with strain at 1138 K (.67 T_m) and a constant strain rate of 3.32×10^{-5} s^{-1} utilizing torsion tests. The testing range was extended to a strain of nearly one. Reciprocal subgrain size was found to continue to decrease past the onset of steady-state while forest dislocation density remained constant throughout steady-state. Data for dislocation spacing in the sub-boundaries was inconclusive, although it appeared that the spacing of dislocations composing the boundaries decreases with steady-state strain and eventually reaches a "saturation" or limiting value. It was concluded that forest dislocations were the significant strengthening feature. Figure 2.2 illustrates their data. Carbide precipitation at the grain boundaries precluded deformation beyond strains of about one.

Only a couple of other investigators deformed specimens to very substantial strains using torsion tests. Schmidt and coworkers [Ref. 18] deformed a ferritic stainless steel to a strain of nearly 16 and found, interestingly, that the subgrain misorientation continuously and dramatically increased with strain. This could be viewed as being consistent with other work that found that d decreased

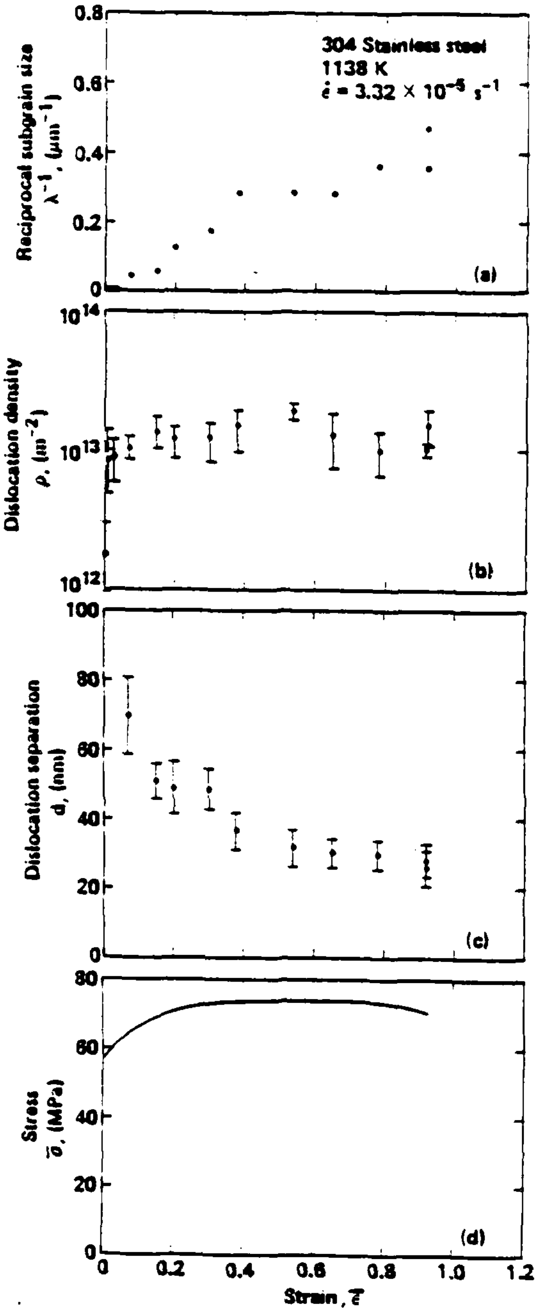

Figure 2.2: Torsional deformation of Type 304 stainless steel at T = 1138 K and $\dot{\varepsilon} = 3.32 \times 10^{-5}\ s^{-1}$. (a) reciprocal subgrain size, λ^{-1}, versus strain, ε; (b) forest dislocation density, ρ, versus ε; (c) subgrain boundary dislocation seperation, d, versus ε; (d) stress, σ, versus ε. (Ref.3)

during steady-state. A recent study by McQueen and coworkers [Ref. 6] deformed aluminum at 673 K (.72 T_m) up to a strain of 60. They found that subgrain size, sub-boundary misorientation, and flow stress remained essentially constant from the onset of steady-state to a strain of sixty. McQueen et. al., however, did not utilize extensive transmission electron microscopy and the results concerning the misorientation across boundaries that form as a result of dislocation accumulation have to be regarded as tentative.

McQueen and coworkers, however, suggest that with very large deformation, the high angle boundaries of the original or annealed metal may increase in total area and be absorbed into the subgrain boundary structure. Subgrain boundaries may be either high or low angle. It was proposed that "geometric dynamic recrystallization" had been responsible for the formation of high angle subgrain boundaries from original grain boundaries which had been serrated, and spiralled to small axial thicknesses.

In the present work, ultra purity (99.999%) aluminum was deformed in torsion at 644 K (0.69 T_m) and an equivalent strain rate of 5.04×10^{-4} s^{-1} to various strains up to 16.33. Deformation of several specimens to these large strain levels would provide a more definite trend in the dislocation microstructure versus strain trends.

Specifically, we were interested whether d (or θ) is constant over the entire range of steady-state creep. If d decreases during steady-state (θ increases) there would be an interest in determining whether a limiting or "saturation" value is reached (suggesting that high angle boundaries don't eventually form from subgrain boundaries). If, as in the earlier torsion work cited, high angle boundaries become increasingly evident at high values of strain, a determination of the origin would be necessary.

III. EXPERIMENTAL PROCEDURE

A. SPECIMEN TESTING AND SAMPLE PREPARATION

Torsion specimens were machined from 99.999% pure, 5/8 inch diameter aluminum rod and then annealed in vacuum for one hour at 698 K. The gage length was 25.4 mm and the gage diameter was 5.1 mm. Specimen deformation was conducted on the Stanford University torsion machine at a constant strain rate of 5.04 x 10^{-4} s^{-1} and a temperature of 644 K. A displacive 99.999% argon gas was passed through the quartz tube surrounding the specimens during heating and deformation. Specimens were quenched by water injected under pressure into the quartz tube. Additional specifications of the Stanford University torsion test machine and specimen test procedures are described in reference four.

Three millimeter diameter disks for the eventual production of TEM thin foils were spark cut from tangentiial slabs cut near the surface (3/4 radius) of the specimen. Disks were ground to a thickness of .45 mm and electropolished using an electrolyte consisting of 469 parts methanol, 25 parts sulfuric acid, and parts hydrofluoric acid at a temperature of -20° C. Thin foils were extracted from twelve specimens deformed from a strain of 0.02 to a strain of 16.33.

The relation:

$$\gamma = \frac{\alpha R}{L_o} \tag{3-1}$$

where, R is the radius, α is the angle of twist, and L_o is the gage length, allows calculation of the shear strain. Similarly, shear stress is determined from the relation:

$$\tau = \frac{M}{2 R} (3 + n + m') \tag{3-2}$$

where, M is the applied twisting moment, n is the strain hardening exponent, and m' is the strain-rate sensitivity exponent. Shear stress, τ, and shear strain, γ, can be converted to equivalent uniaxial stress, σ, and strain, ε, by using the relations:

$$\sigma = \sqrt{3} \gamma \tag{3-3}$$

and

$$\varepsilon = \gamma / \sqrt{3} \tag{3-4}$$

utilizing the Von Mises criterion.

B. TRANSMISSION ELECTRON MISCROSCOPY AND DATA REDUCTION

Transmission electron microscopy was conducted at the Lawrence Livermore National Laboratory utilizing a JEOL

JEM-200 CX transmission electron microscope (TEM) with a biaxial specimen holder (JEOL BST). The spacing of dislocations in the subgrain boundary, d, was determined by maximizing the projected width of the sub-boundary by tilting of the x and y stages of the TEM holder while operating in the bright field (BF) mode. Micrographs for d measurements were taken when at least one set of dislocations was made invisible by operating the TEM under two-beam conditions. The diffraction conditions were set using either a <110> or <211> zone axis and a strong second beam or reciprocal lattice vector (g) that was a <111> type. The magnification of these micrographs was 100,000X. An average value of dislocation spacing, d, for a given strain was determined from, typically, 20 micrographs.

The average value of d for each micrograph was determined using an intercept method with 10 centimeters of total line length drawn perpendicular to the "saw tooth" pattern of the dislocation network. The relation:

$$d = \frac{L}{N_L M} \tag{3-5}$$

was used to calculate d where, M is the magnification, N_L is the number of intersections of the perpendicular lines with the dislocation network, and L is the total line length.

Two typical "saw tooth" images are shown in Figure 3.1. Figure 3.1(a) is a bright field micrograph of two sets of

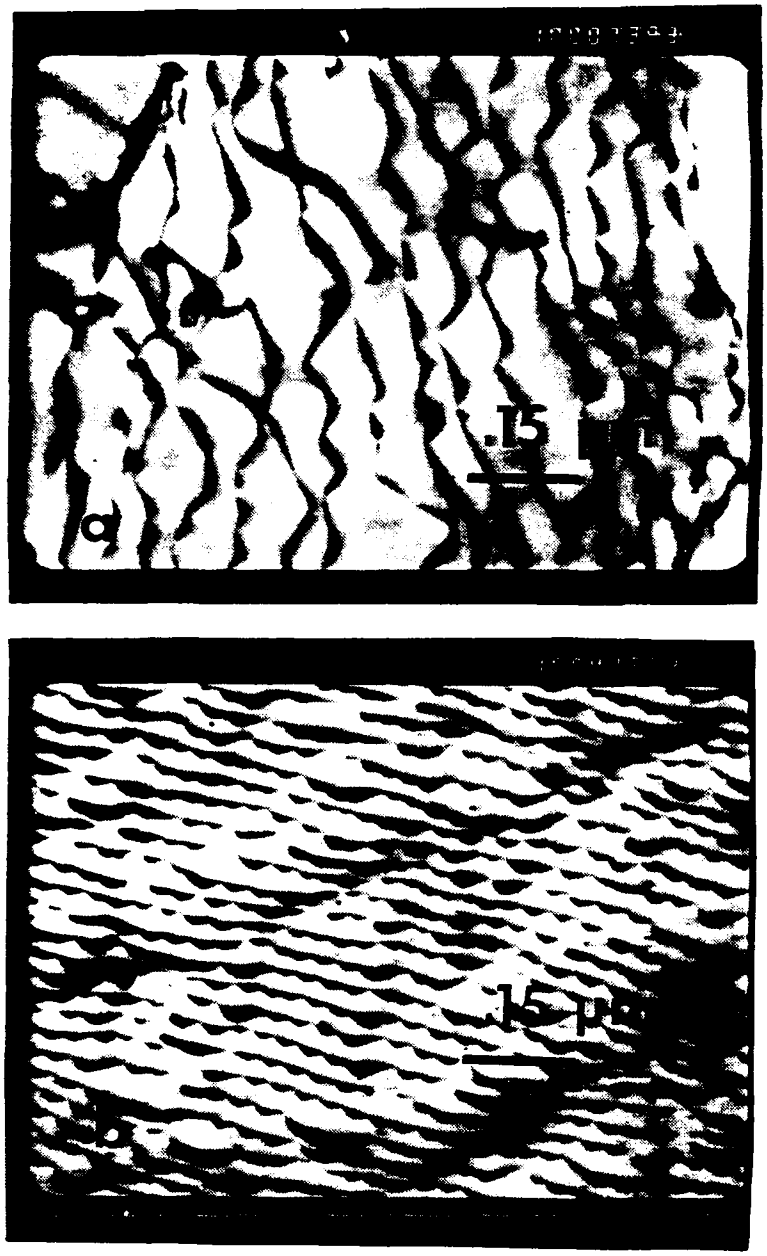

Figure 3.1: Bright field (TEM) micrographs of "saw tooth" patterns in dislocation networks illustrating the variation in dislocation spacing; (a) (211) zone axis with a <111> g vector; (b) (110) zone axis with a <111> g vector. The strain of both specimens was 16.33.

dislocations in the sub-boundary dislocation array with a wide mesh size. One set (approximately perpendicular to the axis of the saw teeth) is invisible. Figure 3.1(b) illustrates a second boundary with a finer mesh size. The strain is 16.33.

Subgrain boundary misorientation across low angle subgrain boundaries was determined by transmission electron microscopy using a Kikuchi line intersection shift method described by Hirsch et. al. [Ref. 19]. The incident beam was positioned to one side of a low-angle boundary while operating the TEM in the bright field mode. Operating in the selected area diffraction (SAD) mode, the foil was tilted slightly to ensure that distinct Kikuchi lines would appear on the photographic plate. One SAD micrograph was taken in this position. A second SAD micrograph was taken after the boundary was traversed. Tilt and rotational components of the low angle boundary were determined by comparison of the two Kikuchi patterns on the glass negatives. The tilt component of misorientation was found by dividing the translation of the pattern by the camera length. The rotational component was measured directly from the glass plates. The net misorientation was determined by using the relation:

$$\cos(\theta) = (\cos a)(\cos b) \tag{3-6}$$

where θ is the net misorientation, a is the tilt misorientation component, and b is the rotational component. Figure 3.2 illustrates a typical diffraction micrograph pair taken across a low angle subgrain boundary.

High angle boundary (HAB) misorientation ($\theta \geq 10^{\circ}$) was determined in a different manner since Kikuchi shifts are too large. The incident beam was positioned on one side of the HAB while operating the TEM in the bright field mode. The foil was tilted while operating in the SAD mode until a reference zone axis, typically (100) or (110), was positioned in the center of the viewing field. After verifying the position of the incident beam on the foil in the BF mode, goniometer readings were recorded for both x and y tilt stages and a SAD micrograph was taken. The boundary was traversed and the foil was tilted to the reference zone axis. A second set of goniometer readings and a second micrograph was taken.

The tilt component of the misorientation was determined by combining the changes in goniometer readings for each stage using Eq. (3-5). The rotational component of misorientation was measured directly from the TEM negatives of the SAD patterns. Eq. (3-5) was used a second time to combine net tilt and rotation to calculate the net misorientation.

When conducting a traverse about the perforation in the TEM foils from strains greater than about 3 or 4, it was

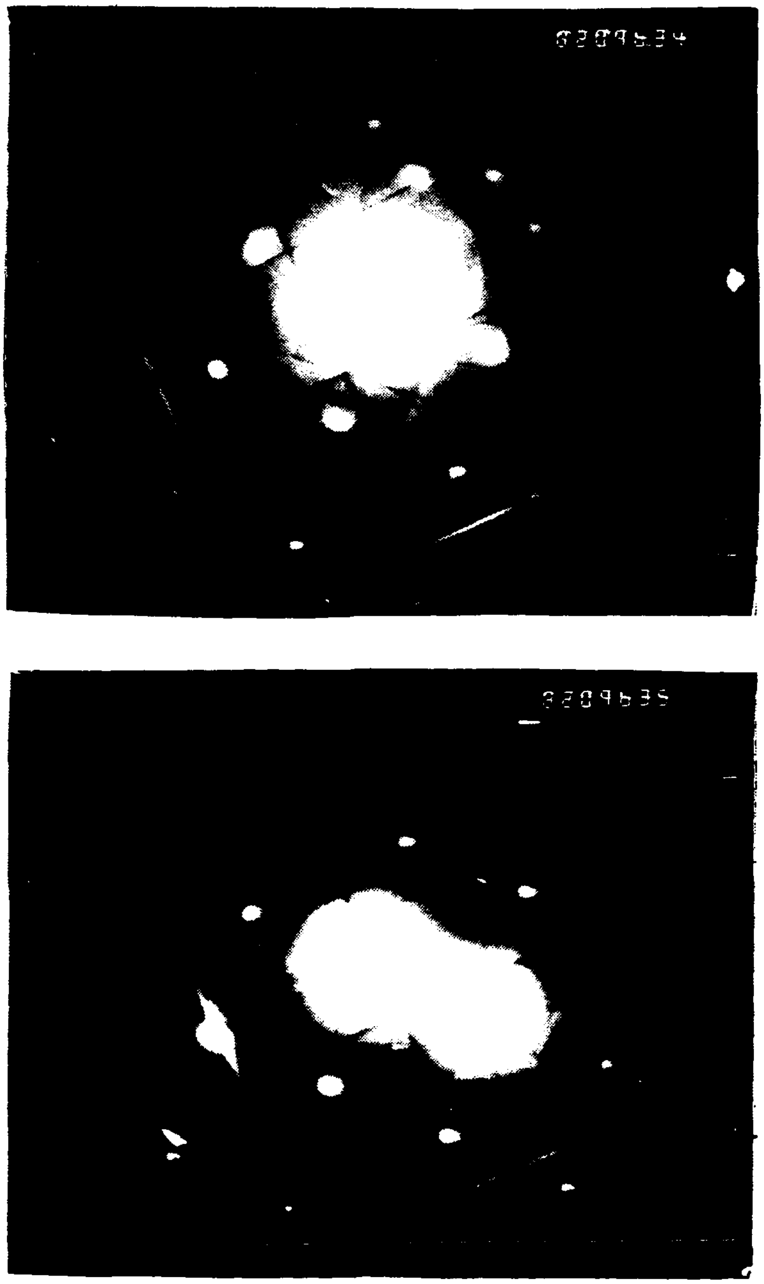

Figure 3.2: Diffraction (TEM) micrograph pair illustrating Kikuchi line shift across a subgrain boundary. Effective camera length was 86.5 cm.

found that approximately one-third of all boundaries were high angle boundaries. For strains greater than or equal to 1.26 (where high angle boundaries are first observed), the average subgrain misorientation across boundaries formed as a result of accumulation of dislocations produced as a result of deformation was computed as the average of all boundaries with misorientation of less than four degrees. Boundaries with greater misorientations than this value were formed from the original grain boundaries by geometric dynamic recrystallization, as discussed earlier.

C. OPTICAL MICROSCOPY

Optical micrographs of samples were taken at Lawrence Livermore National Laboratories from each torsion specimen. Tangential sections were ground with successively finer silicon carbide paper and polished using a diamond paste. Specimens were electropolished in an electrolyte 80 parts methanol and 20 parts nitric acid at a temperature of -20^{o} C. Annodizing was completed using an 8% floroboric acid and 92% water solution at room temperature.

IV. RESULTS AND DISCUSSION

Figure 4.1 shows the stress versus strain behavior of 99.999% pure aluminum at 644 K and an equivalent strain rate of 5.04 x 10^{-4} s^{-1}. The yield stress was found to be 4.24 MPa and peak stress was 7.70 MPa at a strain of 0.20. Despite a 10% reduction (small) in stress that was observed from the peak stress through the range of plastic strain up to about 7, steady-state was considered to be achieved by a strain of 0.20. This drop is less than the 30% reduction reported by McQueen and coworkers [Ref. 6] in a similar deformation study. McQueen attributed the reduction to a texturing effect caused by grains aligning themselves into a "soft" orientation, thus reducing the flow stress. The reduction in flow stress in the present study was attributed to a texturing effect or, perhaps, as a result of grain boundary sliding [Ref. 2].

Results of the direct measurement of dislocation spacing in the sub-boundary network are represented in Figure 4.2. At low values of primary creep strain, ϵ = .03, there are only a few fully developed subgrains and the average spacing of the developed networks in large. The dislocation mesh size decreases rapidly to a value of .064 microns at the onset of steady-state. A constant spacing of roughly .045

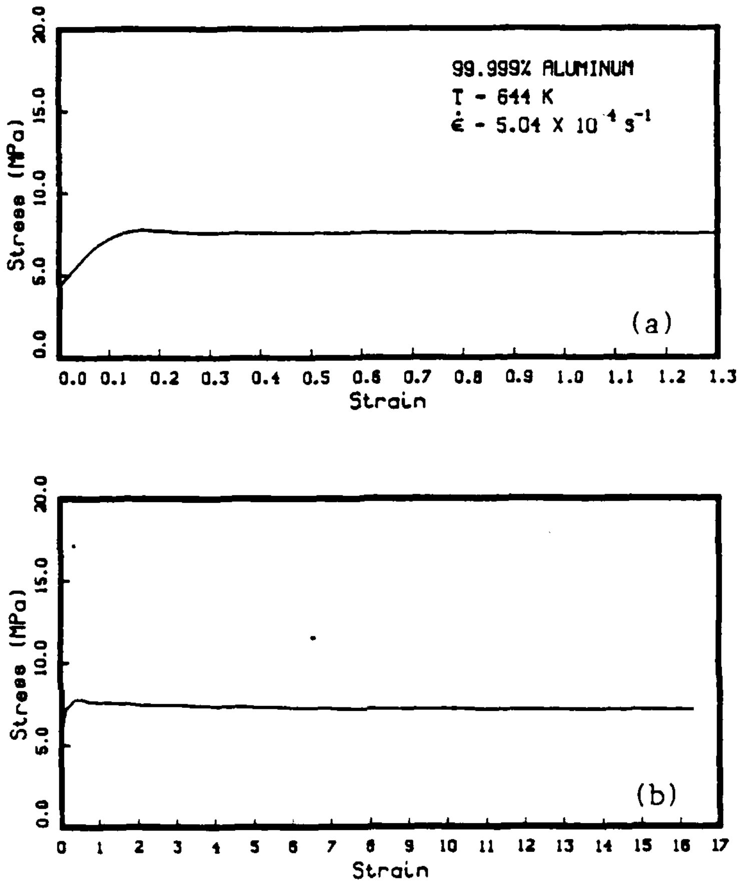

Figure 4.1: Stress versus strain. (a) up to a strain of 1.26; (b) up to a strain of 16.33.

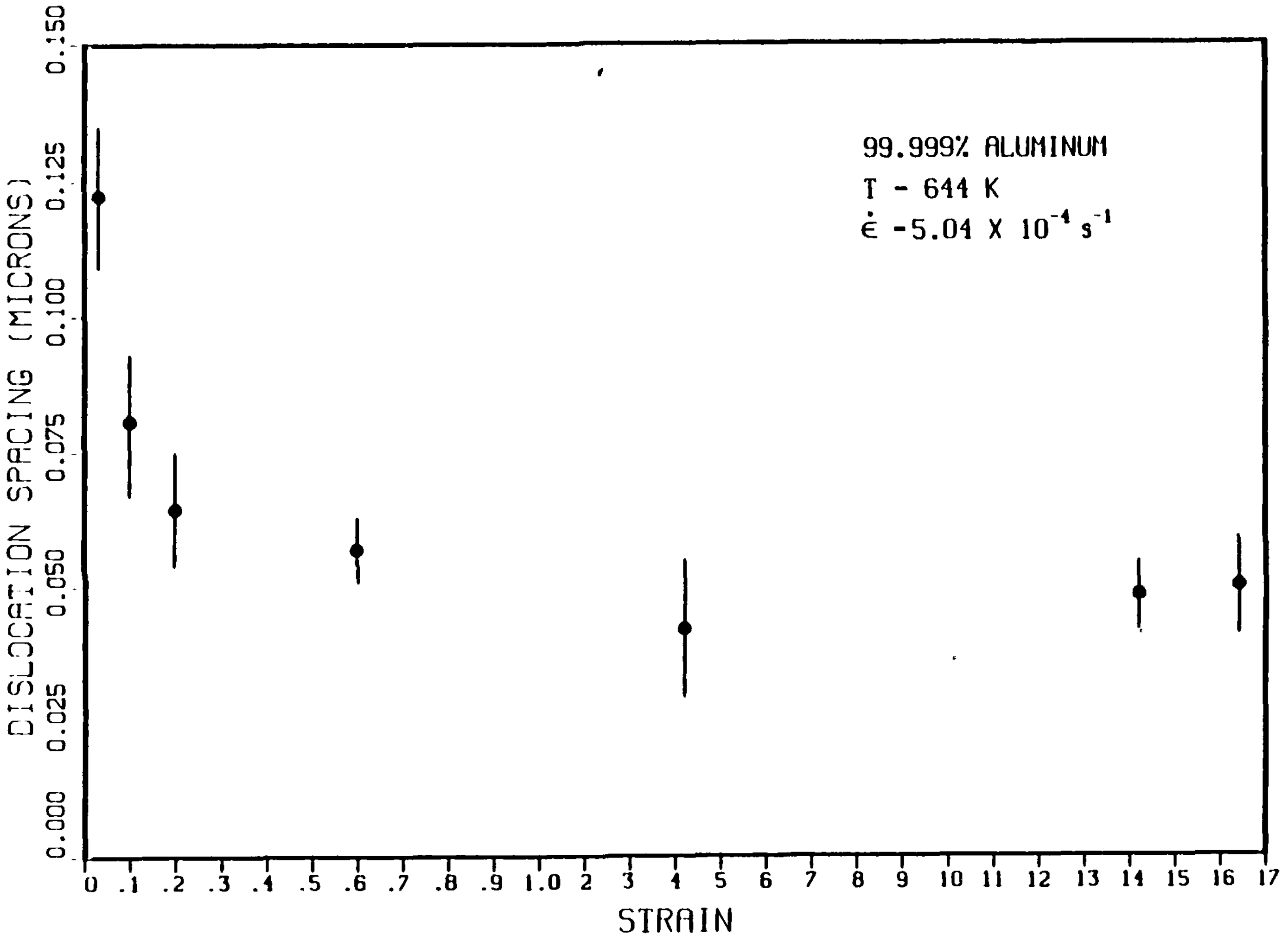

Figure 4.2: Average spacing of dislocations in the subgrain boundary versus strain. The bars on the data points indicate the 95% confidence interval.

microns, however, is not reached until a strain of approximately 1.2, well past steady-state. Although average dislocation spacing decreases dramatically, wide mesh sizes were observed at all values of strain. A similar discovery was made by Petry and Pschenitzka [Ref. 16] in their study of Al-11 wt.% Zn.

Subgrain boundaries seem to absorb (gliding) dislocations over primary and steady-state regimes, which tends to decrease the spacing (increase in θ). After a strain of 1.2, the dissolution or annihilation of existing subgrain boundaries [Ref. 20] and their presumed replacement by new boundaries with larger dislocation spacing balance and a saturation value is reached. This may account for the existence of subgrain boundaries with wide mesh sizes at all strains.

There are limitations to this method of measuring dislocation separation in the subgrain boundary. It was found that dislocation networks could be resolved to a minimum mesh size of only about 10 nm, which corresponds roughly ($\theta = b/d$) to a subgrain misorientation of 1.6 degrees. In boundaries with larger misorientation, it was difficult to discern any dislocation substructure. As a result, the values of d-spacing that were found are thought to be somewhat high at larger strains where subgrain boundaries with misorientations over 1.6 degrees are observed. Therefore, conclusions based on the direct measurement of d are tentative. Results of direct measurements of subgrain misorientation using the kikuchi line shift method are illustrated in Figure 4.3. This method is not dependent on directly imaging dislocation substructure.

Figure 4.3(a) shows the behavior of the average misorientation across low angle ($\theta < 4^{o}$) subgrain boundaries which are believed to form as a result of the accumulation of dislocations produced during creep up to a strain of 1.26. These boundaries are then the "true" subgrain boundaries. Misorientation was observed to increase linearly throughout the entire range of strain. Two previous studies also [Refs. 15, 16] reported a linear increase in subgrain misorientation with strain. Figure 4.3(b) illustrates the behavior of the average subgrain misorientation through the full range of strain. A maximum value of misorientation of approximately 1.15 degrees was reached at a strain of about 1.2, well past steady-state. This data is consistent with the trend of the direct dislocation separation measurements. Both measurements indicate a saturation value of d or θ at about a strain of 1.2 where the dislocation substructure remains fixed with continued deformation.

Figure 4.4 illustrates the distribution of low angle subgrain boundary misorientation data as a function of creep

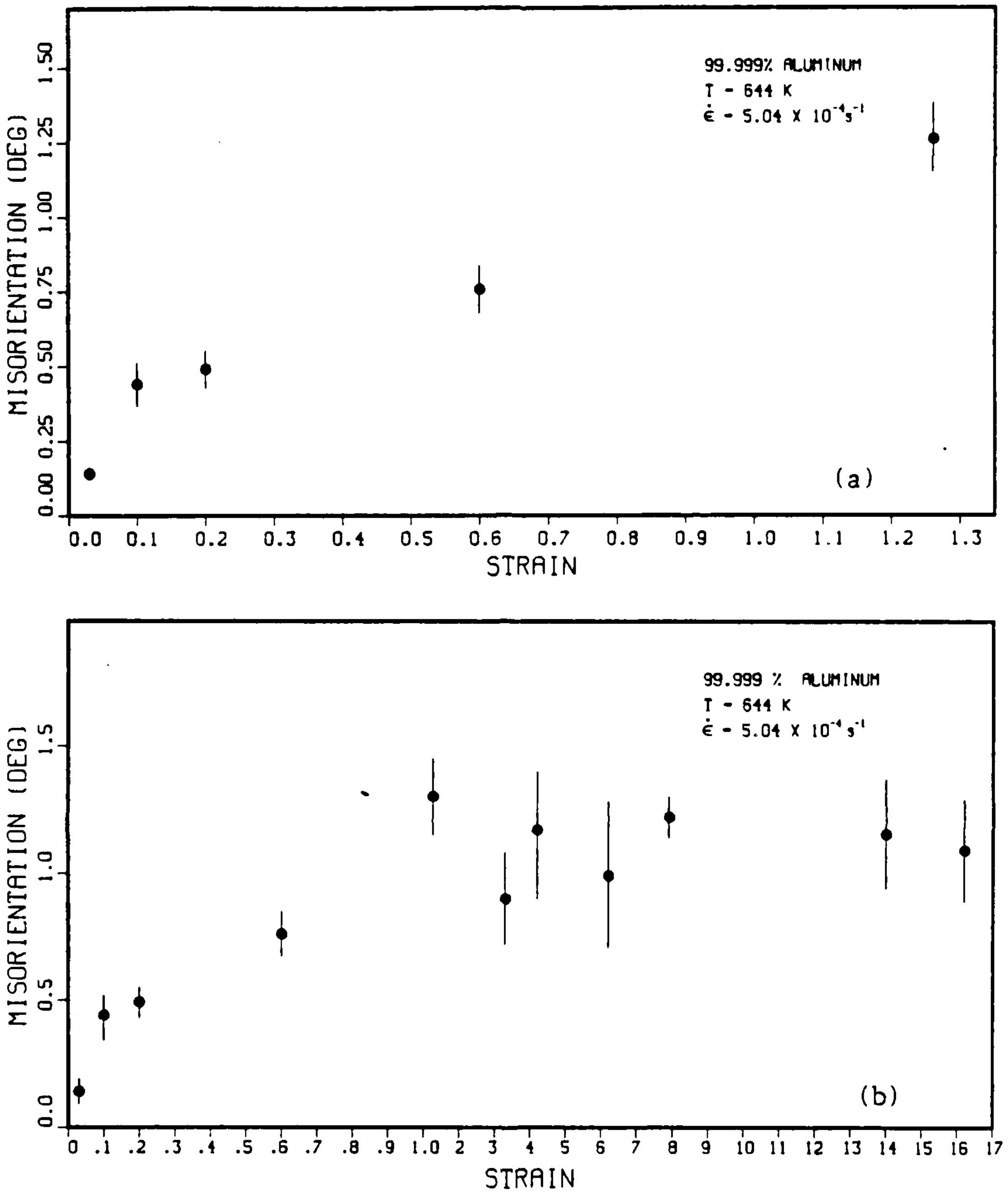

Figure 4.3: Average subgrain misorientation versus strain. (a) to a strain of 1.26; (b) to a strain of 16.33.

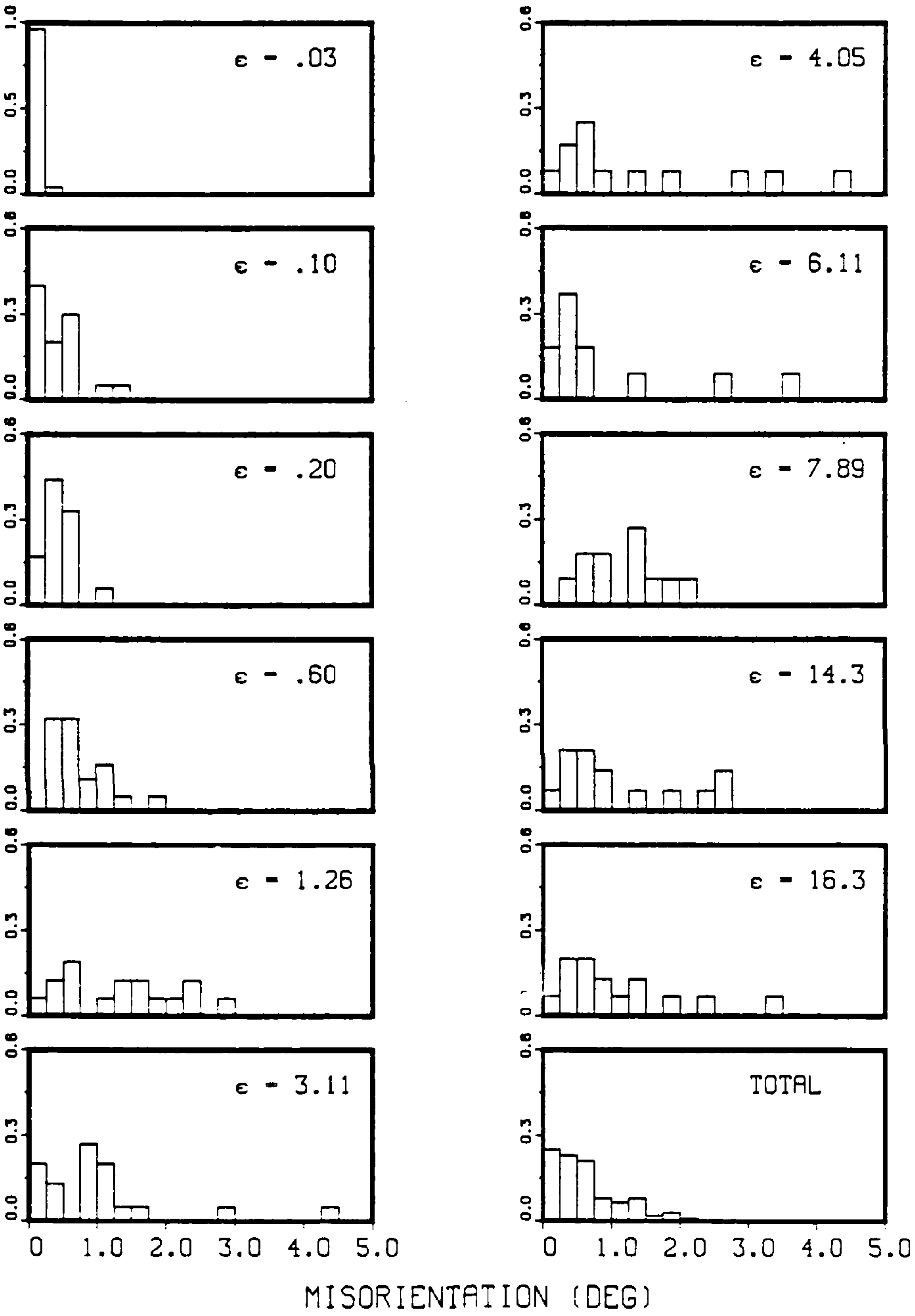

Figure 4.4: The distribution of subgrain misorientation for increasing values of strain.

strain. Initially, all subgrain boundaries have low misorientation. At increasing values of strain, the shape of the distribution flattens out and by a strain of 1.26, the low angle subgrain misorientation angle values were observed in roughly equivalent fractions up to three degrees. There was little evidence of subgrains developing misorientations of over three degrees.

The distribution of misorientation of all subgrain boundaries as a function of strain is shown in Figure 4.5. At low values of strain ($\epsilon < .60$), all boundaries intersected by the traverse around the foil performation are low angle boundaries ($\theta < 3^o$). By a strain of 4.05, one-third of all boundaries intersected were found to be high angle boundaries. These are the boundaries that McQueen and coworkers suggested were the original high angle boundaries of the annealed metal that spiralled around the torsion axis. The axial thickness of the original grains reduced sufficientlly at higher strains so as to become a common appearance in the TEM foils. Therefore, the formation of high angle boundaries at higher strains was not believed to be preceded by a gradual increase in the sub-boundary misorientation. This is confirmed by the fact that the distribution of misorientation was essentially bi-modal with very few boundaries having misorientation angle values between three and nine degrees. The region between three

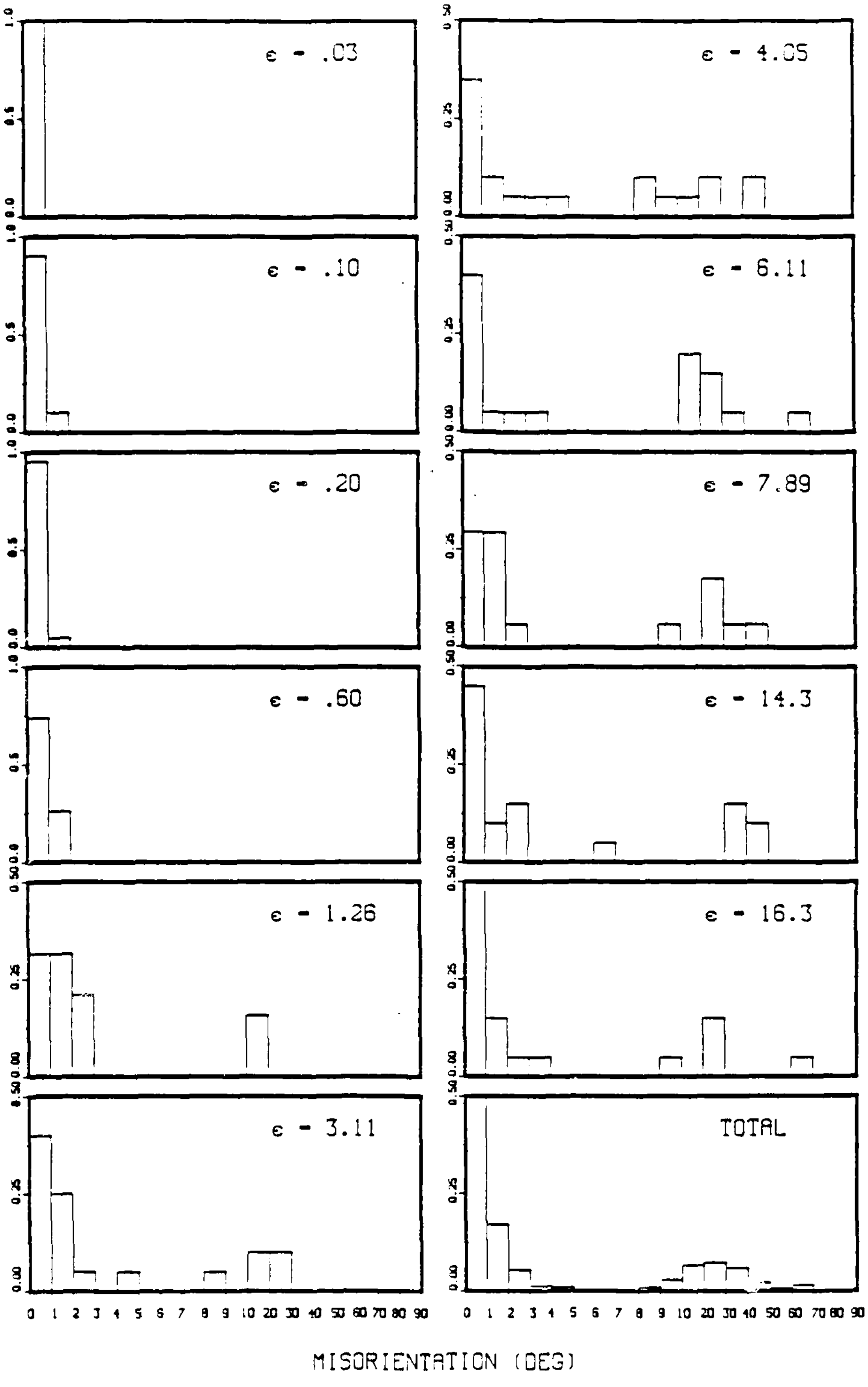

Figure 4.5: Histograms illustrating the distribution of misorientation of all boundaries at increasing values of strain.

and nine degrees would be expected to be well-populated if the misorientation angle of subgrains was continuously increasing to form high angle boundaries.

Polarized light microscopy was conducted to analyze the behavior of the original grain boundaries throughout the range of creep strain to further confirm that the high angle boundaries did not form as a result of a continuous recrystallization (a gradual increase in θ). Figure 4.6 shows six polarized light optical micrographs at increasing values of strain. Figure 4.6(a) was taken from the undeformed grip section of the specimen and shows the original grains. The torsion axis is parallel to the horizontal direction. Figure 4.6(b) shows subgrain formation and a gradual deflection of the original grain boundaries away from the torsion axis at a strain of 0.20. In Figure 4.6(c) (strain of 0.60), subgrains appear more pronounced (due to higher misorientation) and original grain boundaries are increasingly serrated and the axial width of the grains has been reduced. The serrations of the grain boundaries, as discussed earlier, are due to the subgrain formation along the boundaries [Ref. 21]. At a strain of 1.26, Figure 4.6(d), the axial thickness of the grains is further decreased. Figure 4.6(e) is a micrograph of a specimen deformed to a strain of 4.05. Serrated portions of original high angle boundaries appear as short, dark line

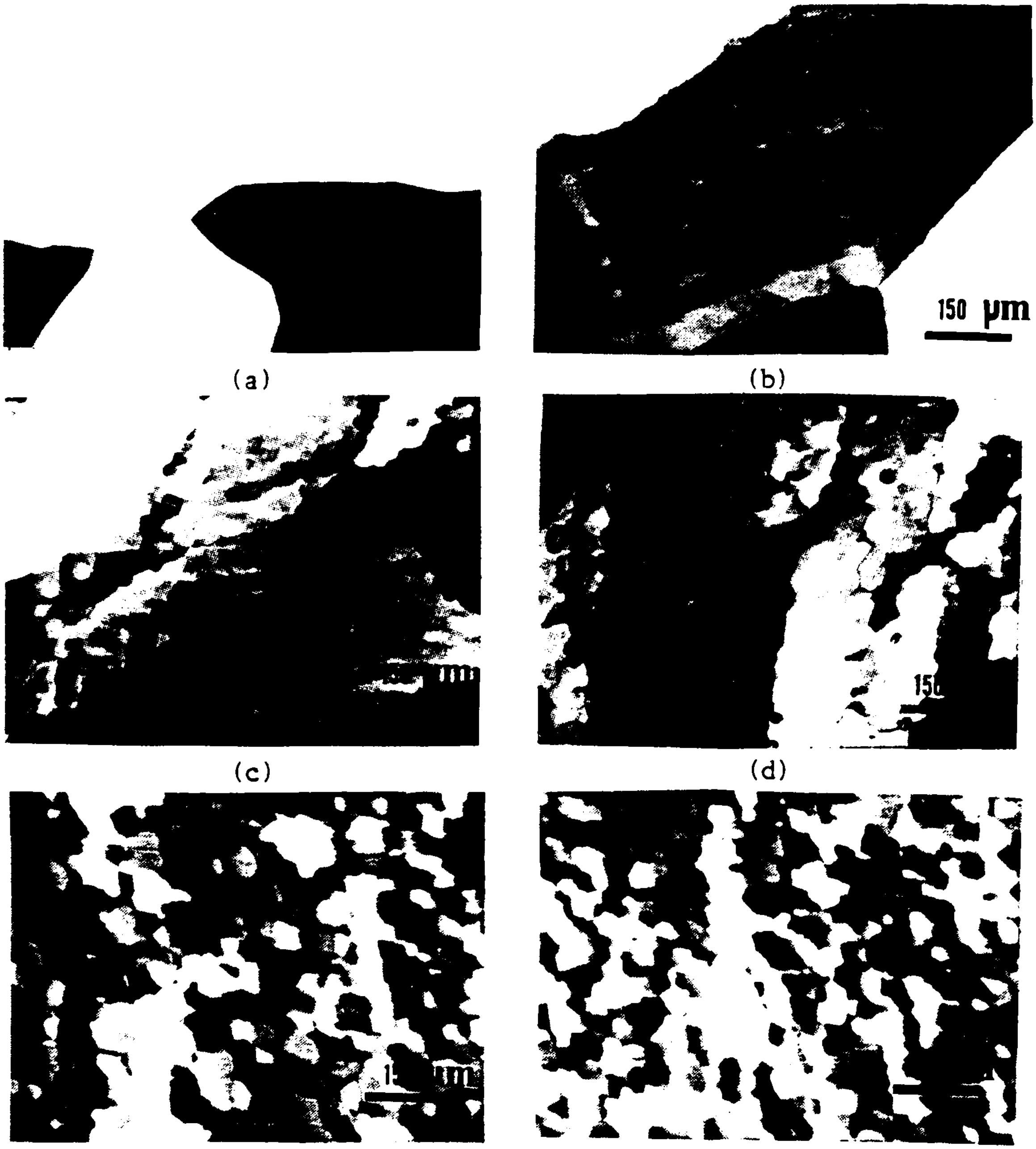

(a) (b) (c) (d) (e) (f)

Figure 4.6: Polarized light optical micrographs of specimens deformed to increasing values of strain. (a) undeformed; (b) at a strain of 0.20; (c) at a strain of 0.60; (d) at a strain of 1.26; (e) at a strain of 4.05; (f) at a strain of 16.33.

segments. The original grains are no longer easily distinguishable as the axial thickness is of the order of the subgrain size. Figure 4.6(f) is a micrograph of a specimen deformed to a strain of 16.33 and the appearance is similar to that of Figure 4.6(e).

Therefore, the evidence from these micrographs suggests that the large number of high angle boundaries at higher values of plastic deformation ($\epsilon > 4.05$) occur as a result of serrated grains that spiral about the torsion axis and are absorbed into the three-dimensional subgrain boundary structure. This conclusion is in complete agreement with conclusions by McQueen and others [Ref. 6] that geometric dynamic recrystallization occurs at large values of plastic strain during the high temperature creep of aluminum.

V. SUMMARY AND CONCLUSIONS

This work was the last part of a comprehensive study of the dislocation microstructure of high purity aluminum deformed to large plastic strains at elevated temperatures. Figure 5.1 summarizes the results of the overall study of microstructural features up to a strain of 1.3 while Figure 5.2 summarizes the results over the full range of strain. In Figures 5.1(a) and (b), subgrain size and forest dislocation density [Refs. 4, 5] remain constant from the onset of steady-state creep throughout the full range of plastic strain. Optical metallography, presented earlier, seemed to confirm the data on subgrain size.

Figure 5.1(c) shows the linear increase in subgrain misorientation up to a strain of about 1.26 (about a factor of six higher strain than that corresponding to the onset of steady-state). Therefore, long after the metal has reached essentially a constant flow stress (strength), features in the sub-boundary network are changing significantly. Whereas the average misorientation of subgrains is roughly 0.60 degrees at the onset of steady-state, the average subgrain misorientation is about 1.15 degrees at a strain of about 1.26. Additionally, beyond a strain of about 3, one-third of all boundaries are high angle boundaries and yet

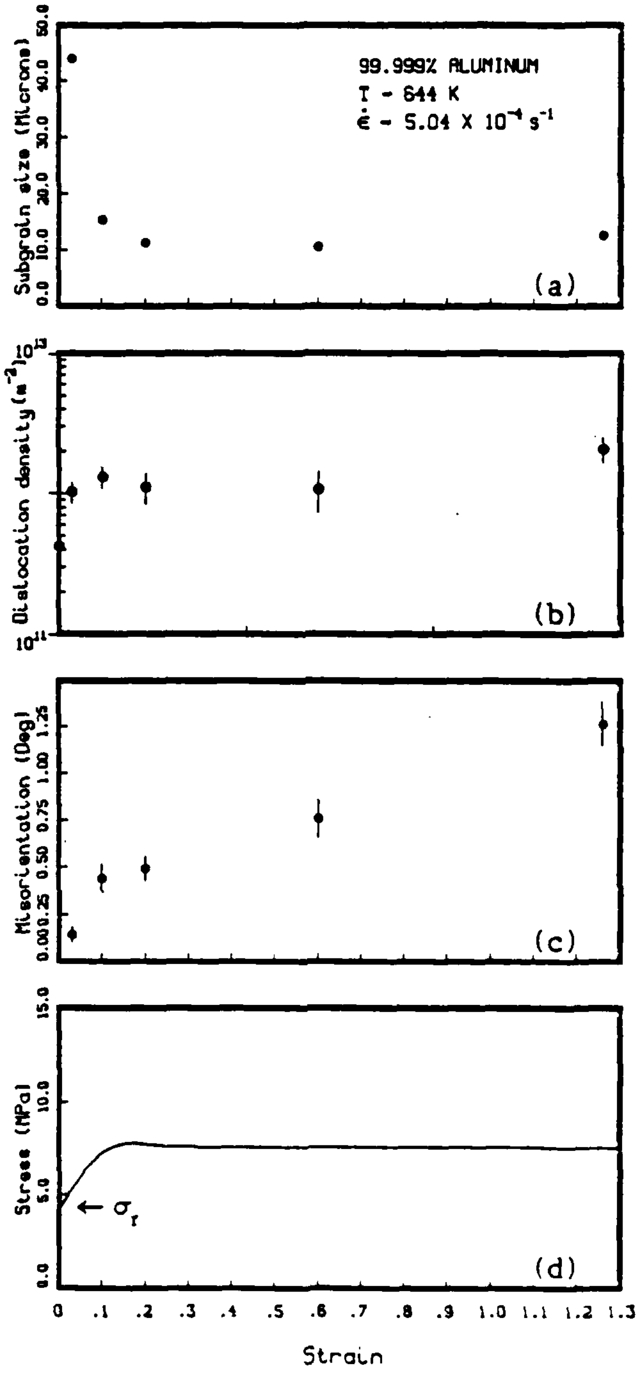

Figure 5.1: Summary of results for torsional deformation to an equivalent strain of 1.3. (a) subgrain size versus strain; (b) forest dislocation density versus strain; (c) subgrain misorientation versus strain; (d) stress versus strain.

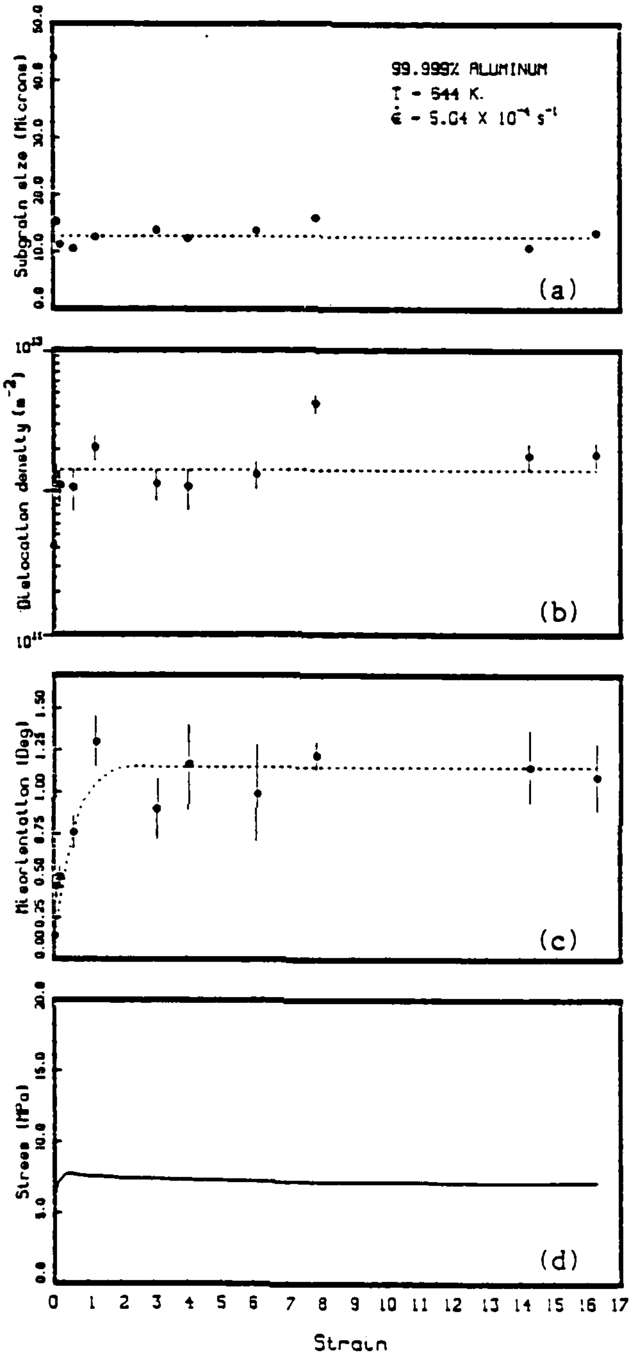

Figure 5.2: Summary of results for torsional deformation to an equivalent strain of 16.33. (a) subgrain size versus strain; (b) forest dislocation density versus strain; (c) subgrain misorientation versus strain; (d) stress versus strain.

there is still no substantial change in flow stress. This further suggests that the details of the sub-boundary do not strongly affect the creep behavior of aluminum.

Models which suggest that d or θ influence the creep rate by changing the distance that edge components of dislocations must climb to annihilate [Refs. 22, 23] imply a substantial change in flow stress with the observed changes in θ during steady-state where a constant stress is actually observed. If, as some models suggest, a decrease in d-spacing improves the ability of the boundary to act as an obstacle to gliding dislocations then an increase in flow stress would be expected based on the findings of this study. Other models [Ref. 15] suggest that the d-spacing is inversely related to the stress at the subgrain boundaries and the stress required to emit dislocations from the sub-boundaries. These also imply a substantial (factor of two or so) change in flow stress with the change in d observed during steady-state in this study.

Evidence from this study suggests that dislocations not associated with subgrain boundaries (forest dislocations) may be primarily responsible for creep strength since ρ does not appear to change over the entire range of steady-state strain. A network theory that was proposed by McLean [Ref. 24] suggests that forest dislocations exist in a three-dimensional network and that creep behavior of subgrain forming metals and alloys is explained in terms of the diffusion controlled network coarsening and the activation of critical sized links as Frank sources of gliding dislocations. Further refinement of network theories is a topic of current research.

LIST OF REFERENCES

1. Sherby, O. D. and Burke, P. M., "Mechanical Behavior of Crystalline Solids at Elevated Temperatures," Progress in Materials Science, Vol. 13, pp. 325-386, 1967.

2. Mukherjee, A. K., "High Temperature Creep," Treatise on Materials Science and Technology, R. J. Arsenault, ed., Vol. 6, p. 163, 1975.

3. Kassner, M. E. and Elmer, J. W., "Variations in the Spacing of Dislocations in Subgrain Boundaries with Creep Strain in Type 304 Stainless Steel," Strength of Metals and Alloys, H. J. McQueen, ed., Pergamon Press, p. 953, 1985.

4. Mieszczanski, P. O., The Variation in the Subgrain Size in Aluminum Deformed to Large Steady-State Creep Strains, M.S. Thesis, Naval Postgraduate School, Monterey, California, September 1985.

5. Wetter, T. S., The Variation of the Dislocation Density in Aluminum Deformed to Large Steady-State Creep Strains, M.S. Thesis, Naval Postgraduate School, Monterey, California, March 1986.

6. McQueen, H. J., Knustad, O., Ryum, N., and Solberg, J. K., "Microstructural Evolution in Aluminum Deformed to Strains of 60 at 400 C," Scripta Metallurgica, Vol. 19, pp. 73-78, 1985.

7. Hu, H., "Direct Observations on the Annealing of a Si-Fe Crystal in the Electron Microscope," Trans. AIME, Vol. 224, pp. 75-84, 1962.

8. Li, J. C., "Possibility of Subgrain Rotation During Recrystallization," Journal of Applied Physics, Vol. 33, pp. 2958-2965, 1962.

9. Dougherty, R. D. and Szpunar, J. A., "Kinetics of Subgrain Coalescence--A Reconsideration of the Theory," Acta Metallurgica, Vol. 32, No. 10, pp. 1789-1798, 1984.

10. Orlova, A., Tobolova, Z., and Cadek, J., "Internal Stress and Dislocation Structure of Aluminum in High-Temperature Creep," Philosophical Magazine, Vol. 26, pp. 1263-1274, 1972.

11. Excell, S. F. and Warrington, D. H., "Subgrain Boundary Migration in Aluminum," Philosophical Magazine, Vol. 4, pp. 1121-1136, 1927.

12. Orlova, A., Tobolova, Z., and Cadek, J., "Dislocation Structure and Applied, Effective and Internal Stress in High-Temperature Creep of Alpha Iron," Philosophical Magazine, Vol. 25, p. 865, 1972.

13. Karashima, S., Oikawa, H., and Hasegawa, T., "Studies on Substructure Developed during Creep Deformation of Copper Crystals," J. Japan Institute of Metals, Vol. 31, p. 782, 1977.

14. Karashima, S., Oikawa, H., and Hasegawa, T., "Transmission Electron Microscopy of Substructures Developed During High Temperature in Alpha Iron," J. Japan Institute of Metals, Vol. 12, p. 369, 1971.

15. Suh, S. H., Cohen, J. B., and Weertman, J., "X-Ray Diffraction Study of Subgrain Misorientation During High Temperature Creep of Tin Single Crystals," Metallurgical Transactions A, Vol. 14A, pp. 117-126, 1983.

16. Morris, M. A. and Martin, J. L., "Microstructural Dependence of Effective Stresses and Activation Volumes During Creep," Acta Metallurgica, Vol. 32, No. 10, pp. 1609-1623, 1984.

17. Petry, F. and Pschenitzka, F., "Evolution of the Dislocation Substructure in an Al-11 wt.% Zn Alloy During Creep," Materials Science and Engineering, Vol. 68, pp. L7-L11, 1984.

18. Schmidt, C. G., Young, C. M., Walser, B., Klundt, R. H., and Sherby, O. D., "The Influence of Substructure on the Elevated and Room Temperature Strength of a 26 Cr-1 Mo Ferritic Stainless Steel," Metallurgical Transactions A, Vol. 13A, p. 447, 1982.

19. Hirsch, P. B. and others, Electron Microscopy of Thin Crystals, pp. 124-128, 509, Butterworths, London, 1969.

20. Calliard, D. and Martin, J. L., "Microstructure of Aluminum During Creep at Intermediate Temperatures--III. The Rate Controlling Process," Acta Metallurgica, Vol. 31, No. 5, pp. 813-825, 1983.

21. Sherby, O. D., Klundt, R. H., and Miller, A. K., "Flow Stress, Subgrain Size, and Subgrain Stability at Elevated Temperature," Metallurgical Transactions A, Vol. 8A, p. 843, 1977.

22. Weertman, J., "Natural Fifth-Power Creep Law for Pure Metals," Proceedings of the Second Conference on Creep and Fracture of Engineering Materials and Structures, p. 1, Pineridge, Swansea, 1984.

23. Blum, W., "Role of Dislocation Annihilation During Steady-State Deformation," Physica Status Solidi B, Vol. 45, p. 561, 1971.

24. McLean, D., "Resistance to Hot Deformation," Trans. AIME, Vol. 224, p. 1193, 1968.

25. Devore, J. L., Probability and Statistics for Engineering and the Sciences, pp. 317-319, Brooks/Cole, 1982.

TABLE I

COMPARATIVE DATA FOR THE COMPREHENSIVE STUDY OF ALUMINUM DEFORMED TO LARGE PLASTIC STRAINS AT 644 K

DATA POINT	TRUE STRAIN	DISLOCATION DENSITY ($10^{12}/m^2$)	SUBGRAIN SIZE (Microns)	SUBGRAIN MISORIENTATION (Degrees)
A-13	0.03	1.03	44.07	0.14
A-6	0.10	1.32	15.35	0.44
A-12	0.20	1.12	11.27	0.49
A-3	0.60	1.08	10.57	0.76
A-4	1.26	2.08	12.60	1.30
A-1	3.11	1.15	13.80	0.90
A-5	4.05	1.09	12.30	1.17
A-11	6.11	1.34	13.73	0.99
A-7	7.89	4.34	15.92	1.22
A-8	13.4	1.82	10.98	1.15
A-9	16.33	1.86	13.47	1.09

APPENDIX A

REDUCED DATA

TABLE A.1

Specimen A-13, ε=.03, T=644 K, $\dot{\varepsilon}=5.04\times10^{-4}s^{-1}$, $\bar{d}$=.122 μm

Foil No.	Micrograph No.	Mag. (10^3)	No. Intercepts for 10 cm of Lines
A-13,2	8862	100 x	16
A-13,2	8863	100 x	7
A-13,2	8864	100 x	9
A-13,2	8865	100 x	5
A-13,2	8866	100 x	9
A-13,2	8867	100 x	9
A-13,2	8868	100 x	7
A-13,2	8869	100 x	6
A-13,2	8871	100 x	8
A-13,2	8872	100 x	20

TABLE A.2

Specimen A-6, $\varepsilon=.103$, $T=644$ K, $\dot{\varepsilon}=5.04\mathrm{x}10^{-4}\mathrm{s}^{-1}$, $\overline{d}=.081$ μm

Foil No.	Micrograph No.	Mag. (10^3)	No. Intercepts for 10 cm of Lines
A-6,1	8885	100 x	17
A-6,1	8886	100 x	18
A-6,1	8887	100 x	13
A-6,1	8888	100 x	14
A-6,1	8889	100 x	13
A-6,1	8890	100 x	8
A-6,8	8873	100 x	11
A-6,8	8874	100 x	18
A-6,8	8875	100 x	15
A-6,8	8876	100 x	17
A-6,8	8877	100 x	17
A-6,8	8878	100 x	7
A-6,8	8879	100 x	7
A-6,8	8880	100 x	10
A-6,8	8881	100 x	13
A-6,9	8894	100 x	16
A-6,12	8882	100 x	18
A-6,12	8883	100 x	32
A-6,12	8884	100 x	13
A-6,12	8891	100 x	18
A-6,12	8892	100 x	9
A-6,12	8893	100 x	8

TABLE A.3

Specimen A-12, $\varepsilon=.20$, T=644 K, $\dot{\varepsilon}=5.04\times10^{-4}s^{-1}$, $\bar{d}=.064$ μm

Foil No.	Micrograph No.	Mag. (10^3)	No. Intercepts for 10 cm of Lines
A-12,1	8910	100 x	19
A-12,1	8912	100 x	9
A-12,1	8913	100 x	15
A-12,1	8914	100 x	12
A-12,1	8915	100 x	18
A-12,1	8916	100 x	12
A-12,2	8907	100 x	12
A-12,2	8908	100 x	22
A-12,2	8910	100 x	19
A-12,2	8924	100 x	22
A-12,2	8925	100 x	12
A-12,2	8926	100 x	16
A-12,2	9540	100 x	36
A-12,2	9541	100 x	47
A-12,2	9542	100 x	20
A-12,2	9543	100 x	12
A-12,2	9544	100 x	14
A-12,2	9545	100 x	19
A-12,2	9546	100 x	8
A-12,2	9547	100 x	32

TABLE A.4

Specimen A-3, ε=.60, T=644 K, $\dot{\varepsilon}$=5.04x$10^{-4}$$s^{-1}$, $\bar{d}$=.057 μm

Foil No.	Micrograph No.	Mag. (10^3)	No. Intercepts for 10 cm of Lines
A-3,1	8929	100 x	22
A-3,1	8930	100 x	13
A-3,1	8931	100 x	18
A-3,1	8932	100 x	14
A-3,1	8933	100 x	22
A-3,1	8934	100 x	21
A-3,1	8935	100 x	12
A-3,1	8936	100 x	25
A-3,2	8911	100 x	20
A-3,11	8963	100 x	32
A-3,11	8964	100 x	14
A-3,11	8965	100 x	32
A-3,11	8966	100 x	57
A-3,12	8917	100 x	24
A-3,12	8918	100 x	25
A-3,12	8921	100 x	12
A-3,12	8922	100 x	15
A-3,12	8923	100 x	17
A-3,13	8927	100 x	11
A-3,13	8928	100 x	11

TABLE A.5

Specimen A-5, ε=4.05, T=644 K, $\dot{\varepsilon}=5.04\times10^{-4}s^{-1}$, $\bar{d}$=.042 μm

Foil No.	Micrograph No.	Mag. (10^3)	No. Intercepts for 10 cm of Lines
A-5,1	8969	100 x	17
A-5,1	8970	100 x	26
A-5,1	8971	100 x	29
A-5,1	8972	100 x	28
A-5,1	8967	100 x	21
A-5,1	8968	100 x	51
A-5,6	7376	100 x	24
A-5,6	7377	100 x	25
A-5,6	7378	100 x	22
A-5,6	7388	100 x	19
A-5,6	7389	100 x	26
A-5,6	7398	100 x	19
A-5,6	7408	100 x	20
A-5,6	7409	100 x	13
A-5,6	7423	100 x	31
A-5,6	7424	100 x	30
A-5,6	7425	100 x	33
A-5,6	7426	100 x	29
A-5,6	7427	100 x	27

TABLE A.6

Specimen A-8, ϵ=14.3, T=644 K, $\dot{\epsilon}=5.04\times10^{-4}s^{-1}$, $\bar{d}$=.0483 μm

Foil No.	Micrograph No.	Mag. (10^3)	No. Intercepts for 10 cm of Lines
A-8,1	9723	100 x	29
A-8,1	9724	100 x	50
A-8,1	9726	100 x	30
A-8,1	9728	100 x	39
A-8,1	9731	100 x	32
A-8,2	9732	100 x	17
A-8,2	9740	100 x	17
A-8,2	9741	100 x	39
A-8,2	9742	100 x	23
A-8,2	9743	100 x	17
A-8,3	9744	100 x	19
A-8,3	9745	100 x	14
A-8,3	9746	100 x	9
A-8,3	9747	100 x	40
A-8,3	9748	100 x	12
A-8,3	9749	100 x	12
A-8,4	9750	100 x	26
A-8,4	9751	100 x	14
A-8,4	9752	100 x	62
A-8,4	9753	100 x	29

TABLE A.7

Specimen A-9, ε=16.33, T=644 K, $\dot{\varepsilon}=5.04\times10^{-4}s^{-1}$, $\bar{d}$=.054 μm

Foil No.	Micrograph No.	Mag. (10^3)	No. Intercepts for 10 cm of Lines
A-9,1	7366	100 x	25
A-9,1	7367	100 x	18
A-9,1	7368	100 x	14
A-9,1	7369	100 x	18
A-9,1	7370	100 x	20
A-9,1	7371	100 x	19
A-9,1	7372	100 x	15
A-9,1	7373	100 x	14
A-9,1	7374	100 x	14
A-9,1	7375	100 x	17
A-9,2	7364	100 x	12
A-9,2	7365	100 x	18
A-9,5	8859	100 x	17
A-9,5	8860	100 x	27
A-9,5	8861	100 x	22
A-9,6	7379	100 x	36
A-9,6	7380	100 x	34
A-9,6	7382	100 x	21
A-9,6	7383	100 x	18
A-9,6	7384	100 x	23
A-9,6	7385	100 x	17

TABLE A.9

Specimen A-6, ϵ=.10, T=644 K, $\dot{\epsilon}=5.04\times10^{-4}s^{-1}$, $\bar{\theta}$=.440(Deg)

Foil No.	Micrograph No.	Displacement for L = 86.5 (cm)	Misorientation Angle (Deg)
A-6,1	9011,9012	0.50	.331
A-6,1	9013,9014	0.25	.166
A-6,1	9015,9016	1.80	1.190
A-6,1	9017,9018	0.90	.596
A-6,1	9019,9020	2.10	1.390
A-6,1	9021,9022	0.25	.166
A-6,8	9023,9024	0.45	.298
A-6,8	9025,9026	0.95	.629
A-6,8	9027,9028	0.25	.166
A-6,8	9029,9030	0.20	.132
A-6,8	9031,9032	0.80	.530
A-6,8	9033,9034	0.25	.166
A-6,8	9035,9036	0.90	.596
A-6,13	9037,9038	0.40	.265
A-6,13	9039,9040	0.35	.232
A-6,13	9041,9042	0.90	.596
A-6,13	9043,9044	0.65	.431
A-6,13	9045,9046	0.30	.199
A-6,13	9047,9048	1.05	.695
A-6,13	9049,9050	0.20	.132
A-6,13	9051,9052	0.50	.331

TABLE A.10

Specimen A-12, $\varepsilon=.20$, $T=644$ K, $\dot{\varepsilon}=5.04\times10^{-4}s^{-1}$, $\bar{\theta}=.492$(Deg)

Foil No.	Micrograph No.	Displacement for L = 86.5 (cm)	Misorientation Angle (Deg)
A-12,2	9053,9054	0.60	.397
A-12,2	9055,9056	1.00	.662
A-12,2	9057,9058	0.20	.132
A-12,2	9059,9060	0.50	.331
A-12,2	9061,9062	0.60	.397
A-12,2	9063,9064	1.00	.662
A-12,2	9065,9066	0.80	.530
A-12,2	9067,9068	1.05	.695
A-12,2	9069,9070	0.35	.232
A-12,2	9071,9072	0.80	.530
A-12,2	9073,9074	0.70	.464
A-12,2	9075,9076	1.05	.695
A-12,2	9079,9080	0.30	.199
A-12,2	9080,9081	1.55	1.020
A-12,2	9041,9042	0.70	.464
A-12,2	9043,9044	0.65	.431
A-12,2	9045,9046	0.60	.397
A-12,2	9047,9048	0.70	.464
A-12,2	9049,9050	0.70	.464
A-12,2	9051,9052	1.00	.662

TABLE A.11

Specimen A-3, $\varepsilon=.60$, T=644 K, $\dot{\varepsilon}=5.04\times10^{-4}s^{-1}$, $\bar{\theta}=.760$ (Deg)

Foil No.	Micrograph No.	Displacement for L = 86.5 (cm)	Misorientation Angle (Deg)
A-3,2	9153,9154	1.10	.723
A-3,2	9155,9156	1.70	1.126
A-3,2	9157,9158	2.00	1.325
A-3,2	9159,9160	1.40	.927
A-3,2	9161,9162	1.80	1.192
A-3,2	9163,9164	0.80	.530
A-3,12	9165,9166	1.40	.927
A-3,12	9167,9168	0.80	.530
A-3,12	9169,9170	0.50	.331
A-3,12	9171,9172	0.80	.530
A-3,12	9173,9174	0.70	.464
A-3,12	9175,9176	0.50	.331
A-3,12	9177,9178	0.60	.397
A-3,12	9179,9180	0.75	.497
A-3,12	9181,9182	2.70	1.788
A-3,12	9183,9184	1.10	.723
A-3,12	9185,9186	1.00	.662
A-3,12	9187,9188	0.50	.331
A-3,12	9189,9190	1.64	1.092

TABLE A.12

Specimen A-4, $\varepsilon=1.26$, T=644 K, $\dot{\varepsilon}=5.04\times10^{-4}s^{-1}$

Foil No.	Micrograph No.	Camera Length	Net Misorientation Angle (Deg)
A-4,5	9194,9195	86.5 cm	17.06
A-4,5	9196,9197	86.5 cm	.25
A-4,5	9198,9199	86.5 cm	.63
A-4,5	9200,9201	86.5 cm	1.01
A-4,5	9202,9203	86.5 cm	2.14
A-4,5	9204,9205	86.5 cm	.74
A-4,5	9206,9207	86.5 cm	1.94
A-4,5	9208,9209	86.5 cm	15.42
A-4,5	9210,9211	86.5 cm	2.89
A-4,5	9212,9213	86.5 cm	.46
A-4,5	9214,9215	86.5 cm	2.39
A-4,5	9216,9217	86.5 cm	.33
A-4,5	9218,9219	86.5 cm	1.66
A-4,5	9220,9221	86.5 cm	1.28
A-4,5	9222,9223	86.5 cm	.75
A-4,5	9224,9225	86.5 cm	1.29
A-4,5	9226,9227	86.5 cm	10.60
A-4,5	9228,9229	86.5 cm	2.40
A-4,5	9230,9231	86.5 cm	1.62

TABLE A.13

Specimen A-1, $\epsilon=3.11$, T=644 K, $\dot{\epsilon}=5.04\times10^{-4}s^{-1}$

Foil No.	Micrograph No.	Camera Length	Net Misorientation Angle (Deg)
A-1,10	9234,9235	86.5 cm	1.43
A-1,10	9236,9237	86.5 cm	.13
A-1,10	9238,9239	86.5 cm	1.16
A-1,10	9240,9241	86.5 cm	11.98
A-1,10	9242,9243	86.5 cm	1.03
A-1,10	9244,9245	86.5 cm	.83
A-1,10	9246,9247	86.5 cm	17.49
A-1,10	9248,9249	86.5 cm	2.90
A-1,10	9250,9251	86.5 cm	.86
A-1,10	9252,9253	86.5 cm	1.68
A-1,10	9254,9255	86.5 cm	.76
A-1,10	9256,9257	86.5 cm	4.48
A-1,10	9258,9259	86.5 cm	29.03
A-1,10	9260,9261	86.5 cm	.33
A-1,10	9262,9263	86.5 cm	.82
A-1,10	9264,9265	86.5 cm	.40
A-1,10	9266,9267	86.5 cm	8.40
A-1,10	9268,9269	86.5 cm	20.16
A-1,10	9270,9271	86.5 cm	.13
A-1,10	9272,9273	86.5 cm	1.23

TABLE A.14

Specimen A-5, $\varepsilon=4.05$, T=644 K, $\dot{\varepsilon}=5.04\times10^{-4}s^{-1}$

Foil No.	Micrograph No.	Camera Length	Net Misorientation Angle (Deg)
A-5,3	0390,0391	86.5 cm	41.40
A-5,3	9634,9635	86.5 cm	.80
A-5,3	9636,9637	86.5 cm	.27
A-5,3	9638,9639	86.5 cm	2.78
A-5,3	9640,9641	86.5 cm	.60
A-5,3	9642,9643	86.5 cm	31.34
A-5,3	9644,9645	86.5 cm	4.50
A-5,3	0384,0385	86.5 cm	28.70
A-5,3	9648,9649	86.5 cm	1.91
A-5,3	9650,9651	86.5 cm	1.39
A-5,3	9652,9653	86.5 cm	.33
A-5,3	9654,9655	86.5 cm	.20
A-5,3	0388,0389	86.5 cm	11.40
A-5,3	9658,9659	86.5 cm	.65
A-5,3	9660,9661	86.5 cm	16.20
A-5,3	9662,9663	86.5 cm	8.46
A-5,3	9664,9665	86.5 cm	3.43
A-5,3	9666,9667	86.5 cm	11.80
A-5,3	9668,9669	86.5 cm	8.80
A-5,3	9670,9671	86.5 cm	.53

TABLE A.15

Specimen A-11, $\varepsilon=6.11$, $T=644$ K, $\dot{\varepsilon}=5.04\times10^{-4}s^{-1}$

Foil No.	Micrograph No.	Camera Length	Net Misorientation Angle (Deg)
A-11,4	9680,9681	86.5 cm	26.40
A-11,4	9682,9683	86.5 cm	.39
A-11,4	9684,9685	86.5 cm	16.12
A-11,4	9686,9687	86.5 cm	33.50
A-11,4	9688,9689	86.5 cm	.60
A-11,4	0414,0415	86.5 cm	10.09
A-11,4	0408,0409	86.5 cm	11.40
A-11,4	9694,9695	86.5 cm	.14
A-11,4	9696,9697	86.5 cm	3.56
A-11,4	9698,9699	86.5 cm	1.46
A-11,4	0412,0413	86.5 cm	10.07
A-11,4	9702,0703	86.5 cm	27.17
A-11,4	9704,9705	86.5 cm	42.20
A-11,4	9706,9707	86.5 cm	2.71
A-11,4	9708,9709	86.5 cm	.33
A-11,4	9710,9711	86.5 cm	.45
A-11,4	0410,0411	86.5 cm	67.97
A-11,4	9714,9715	86.5 cm	.71
A-11,4	9716,9717	86.5 cm	.35
A-11,4	9718,9719	86.5 cm	.14

TABLE A.16

Specimen A-7, $\epsilon=7.89$, T=644 K, $\dot{\epsilon}=5.04\times10^{-4}s^{-1}$

Foil No.	Micrograph No.	Camera Length	Net Misorientation Angle (Deg)
A-7,10	9275,9276	86.5 cm	.81
A-7,10	9277,9278	86.5 cm	1.84
A-7,10	9279,9280	86.5 cm	1.70
A-7,10	9281,9282	86.5 cm	27.52
A-7,10	9283,9284	86.5 cm	1.44
A-7,10	9285,9286	86.5 cm	42.40
A-7,10	9287,9288	86.5 cm	.73
A-7,10	9289,9290	86.5 cm	9.80
A-7,10	9291,9292	86.5 cm	20.17
A-7,10	9293,9294	86.5 cm	1.35
A-7,10	9295,9296	86.5 cm	2.17
A-7,10	9297,9298	86.5 cm	34.00
A-7,10	9299,9300	86.5 cm	.45
A-7,10	9301,9302	86.5 cm	.67
A-7,10	9303,9304	86.5 cm	25.40
A-7,10	9305,9306	86.5 cm	1.26
A-7,10	9307,9308	86.5 cm	.96

TABLE A.17

Specimen A-8, $\varepsilon=14.3$, $T=644$ K, $\dot{\varepsilon}=5.04\times10^{-4}s^{-1}$

Foil No.	Micrograph No.	Camera Length	Net Misorientation Angle (Deg)
A-8,5	9500,9501	86.5 cm	.13
A-8,5	0398,0399	86.5 cm	44.10
A-8,5	0404,0405	86.5 cm	38.00
A-8,5	9506,9507	86.5 cm	.36
A-8,5	0402,0403	86.5 cm	40.00
A-8,5	9510,9511	86.5 cm	.94
A-8,5	9512,9513	86.5 cm	.73
A-8,5	9514,9515	86.5 cm	1.89
A-8,5	0406,0407	86.5 cm	35.80
A-8,5	0400,0401	86.5 cm	34.10
A-8,5	9520,9521	86.5 cm	6.60
A-8,5	9522,9523	86.5 cm	.69
A-8,5	9524,9525	86.5 cm	.97
A-8,5	9526,9527	86.5 cm	.69
A-8,5	9528,9529	86.5 cm	.48
A-8,5	9530,0531,	86.5 cm	2.70
A-8,5	9532,9533	86.5 cm	2.34
A-8,5	9534,9535	86.5 cm	1.31
A-8,5	9536,9537	86.5 cm	.36
A-8,5	9538,9539	86.5 cm	2.54

TABLE A.18

Specimen A-9, $\varepsilon=16.33$, T=644 K, $\dot{\varepsilon}=5.04\mathrm{x}10^{-4}\mathrm{s}^{-1}$

Foil No.	Micrograph No.	Camera Length	Net Misorientation Angle (Deg)
A-9,5	9460,9461	86.5 cm	.72
A-9,5	0396,0397	86.5 cm	23.40
A-9,5	9464,9465	86.5 cm	1.81
A-9,5	0394,0395	86.5 cm	21.10
A-9,5	9468,9469	86.5 cm	.86
A-9,5	9470,9471	86.5 cm	1.00
A-9,5	9472,9473	86.5 cm	.72
A-9,5	9474,9475	86.5 cm	.75
A-9,5	9476,9477	86.5 cm	.56
A-9,5	9478,9479	86.5 cm	2.38
A-9,5	9280,9281	86.5 cm	23.85
A-9,5	9482,9483	86.5 cm	1.36
A-9,5	0392,0393	86.5 cm	63.80
A-9,5	9486,9487	86.5 cm	.33
A-9,5	9488,9489	86.5 cm	.23
A-9,5	9490,9491	86.5 cm	9.80
A-9,5	9492,9493	86.5 cm	1.36
A-9,5	9494,9495	86.5 cm	.33
A-9,5	9496,9497	86.5 cm	3.34
A-9,5	9498,9499	86.5 cm	.45

TABLE A.19

Specimen A-12, $\epsilon=.02$, T=644 K, $\dot{\epsilon}=5.04\times10^{-4}s^{-1}$

Foil No.	Micrograph No.	Mag. (10^3)	No. Dislocations
A-12,1	10185	20 x	20
A-12,1	10184	20 x	20
A-12,1	10191	20 x	53
A-12,1	10192	20 x	59
A-12,1	10187	20 x	32
A-12,1	10188	20 x	30
A-12,1	10189	20 x	16
A-12,1	10200	20 x	20
A-12,1	10201	20 x	16
A-12,1	10197	20 x	37
A-12,1	10198	20 x	22
A-12,1	10186	20 x	27
A-12,1	10205	20 x	41
A-12,1	10202	20 x	29
A-12,1	10203	20 x	37
A-12,1	10204	20 x	36
A-12,1	10193	20 x	18
A-12,1	10190	20 x	29
A-12,1	10199	20 x	20

APPENDIX B

CONFIDENCE INTERVAL DETERMINATION

To determine the error for any level of confidence, the sample set of data is assumed to constitute a random sample from a normal distribution. The standard normal variable is:

$$Z = \frac{\overline{X} - \mu}{\sigma / \sqrt{n}} \qquad \text{(B-1)}$$

where, σ is the standard deviation, n is the sample size, μ is the expected value, and X is the sample mean.

If the desired level of confidence is 95%, then since 95% of the area under the standard normal curve (or .95) is found between the values -1.96 to 1.96:

$$P\left(-1.96 \leq \frac{\overline{X} - \mu}{\sigma / \sqrt{n}} \leq 1.96 \right) = .95 \qquad \text{(B-2)}$$

(Note: Any confidence interval may be chosen. The only values to change in the above equation are the values which enclose the percent area under the standard normal curve corresponding to the level of confidence.) Rewriting Eq. B-2:

$$P\ (\bar{X} - 1.96\ \sigma/\sqrt{n} < \mu < \bar{X} + 1.96\ \sigma/\sqrt{n}) \doteq .95 \qquad \text{(B-3)}$$

and the 95% confidence interval is the length between:

$$\bar{X} \pm \frac{1.96\ \sigma}{\sqrt{n}} \qquad \text{(B-4)}$$

Therefore, the probability is .95 that the interval includes or covers the true value of μ. [Ref. 25]

INITIAL DISTRIBUTION LIST

		No. Copies
1.	Defense Technical Information Center Cameron Station Alexandria, Virginia 22304-6145	2
2.	Library, Code 0142 Naval Postgraduate School Monterey, California 93943-5000	2
3.	Department Chairman, Code 69Mx Department of Mechanical Engineering Naval Postgraduate School Monterey, California 93943-5000	1
4.	Professor M. E. Kassner, Code 69Km Department of Mechanical Engineering Naval Postgraduate School Monterey, California 93943-5000	5
4.	Commanding Officer, Code 330 Supervisor of Shipbuilding Conversion and Repair Attn: LT M. E. McMahon San Francisco, California 94135-2996	4

END

1-87

DTIC